



HAL
open science

Comparison of various 3D pore space reconstruction methods and implications on transport properties of nanoporous rocks

Anne-Julie Tinet, Quentin Corlay, Pauline Collon, Fabrice Golfier, Kassem Kalo

► To cite this version:

Anne-Julie Tinet, Quentin Corlay, Pauline Collon, Fabrice Golfier, Kassem Kalo. Comparison of various 3D pore space reconstruction methods and implications on transport properties of nanoporous rocks. *Advances in Water Resources*, 2020, 141, pp.103615. 10.1016/j.advwatres.2020.103615 . hal-02917323

HAL Id: hal-02917323

<https://hal.univ-lorraine.fr/hal-02917323v1>

Submitted on 14 Oct 2020

HAL is a multi-disciplinary open access archive for the deposit and dissemination of scientific research documents, whether they are published or not. The documents may come from teaching and research institutions in France or abroad, or from public or private research centers.

L'archive ouverte pluridisciplinaire **HAL**, est destinée au dépôt et à la diffusion de documents scientifiques de niveau recherche, publiés ou non, émanant des établissements d'enseignement et de recherche français ou étrangers, des laboratoires publics ou privés.

Comparison of various 3D pore space reconstruction methods and implications on transport properties of nanoporous rocks

Anne-Julie Tinet¹, Quentin Corlay¹, Pauline Collon¹, Fabrice Golfier¹, and Kassem Kalo¹

¹Université de Lorraine, CNRS, GeoRessources laboratory, F-54000 Nancy, France

Abstract Understanding fluid flow and transport within clay rock is essential for predicting caprock integrity in underground gas storage or as host rock in deep radioactive waste storage. The connectivity and topology of the nanopore space, which drive the transfer mechanisms of these materials, are still poorly known and direct 3D imaging is particularly challenging. In this work, we investigate and compare different stochastic reconstruction approaches based on two-point and multiple-point statistics (MPS) methods and using information from 2D training images for 3D volume rendering at submicron scale. A particular emphasis is given to the maximal critical distance of sampling between two consecutive 2D images which is necessary to obtain a coherent 3D reconstruction of the nanopore structure. We assess how these realizations honour various crucial transport properties of material, namely permeability, effective diffusion and longitudinal dispersion. Morphological features such as pore volume, specific surface, Euler characteristic and tortuosity are used to analyze the results. The methods are employed on a synthetic clay of nanometric porosity for which FIB-SEM images are available. Results indicate that the 3DA-MPS and weighted-3DA-MPS approaches are the most suited for preserving pore space features and transport properties, the choice depending on the level of conditioning data available.

Keywords

nanoporous rock
digital rock physics
MPS method
transport property
lattice Boltzmann simulation

Characterization of transport and retention properties of argillaceous rocks in the context of underground storage is a crucial topic for assessing the gas storage capacity or the reliability of long-term evolution scenarios for radioactive wastes [e.g. [Marschall et al., 2005](#)]. It requires to determine with great precision their macroscopic properties (e.g., intrinsic permeability, retention curve, relative permeability, effective diffusion) but the experimental acquisition of these data can be particularly challenging and time-consuming and, in some instances, even unreliable due to intrinsic couplings with other physical processes or damages of the rock samples during essays. There is therefore a very serious hope to significantly improve the characterization of these properties digitally by taking full advantage of advances in imaging at different scales [[Andrä et al., 2013a,b](#)]. This is the aim of the so-called Digital Rock Physics (DRP) approach based on the use of high resolution digital images of rocks so that the material properties are evaluated numerically at the pore scale [[Blunt et al., 2013](#), [Guibert et al., 2015](#), [Tahmasebi et al., 2017c](#), [Shiota et al., 2019](#)].

In addition to classical indirect methods such as mercury intrusion porosimetry (MIP) or nuclear magnetic resonance relaxometry which give only access to pore size distribution, the recent evolution of visualization techniques (micro X-ray computed Tomography or μ -CT, in particular) of 3D porous networks has led to an ever more detailed understanding of the pore structure [[Blunt et al., 2013](#), [Wildenschild and Sheppard, 2013](#), [Rozenbaum and du Roscoat, 2014](#)]. However, the very low permeability materials have nanometric and micrometric

pores whose μ -CT description is still fragmented given the current technological limitations (maximum accessible resolution within the micrometric range). Moreover, a great care must be exercised to capture the pore geometry at the appropriate scale since the connectivity and topology of the pores play a particularly important role in driving the transfer mechanisms for these hygroscopic materials [[Hu et al., 2012](#)]. Indeed, although they may have a significant overall porosity (e.g., of the order of 18-20% for argillite), more than 90% consists of pores smaller than 100 nm (micro- and mesopores) whose architecture remains poorly known. Their connectivity (or not) will contribute for instance to a more or less marked hysteresis during the drainage-imbibition cycles whereas the shape of these pores can modify the transfer conditions locally.

Scanning Electron Microscopy (SEM) is still the most appropriate approach to obtain information on mesoporosity. Recent advances in BIB or FIB (Broad- or Focused-Ion Beam) methods have resulted in series of nanometer-thick slices that can be imaged with SEM to characterize the 3D pore space at a very high resolution level [[Holzer et al., 2010](#), [Desbois et al., 2014](#), [Hemes et al., 2015](#), [Song et al., 2015](#)]. However, besides the fact that it is a destructive method, a better resolution implies a smaller studied volume and thus an increased difficulty to visualize a representative elementary volume (REV) and hence, the interactions between nano- and micro-pores [[Mehmani and Prodanović, 2014](#)]. The FIB-SEM method is in fact constrained by the size of the 3D sample to be analyzed, of the order of a few hundreds of μm^3 , which remains generally lower than the REV [[Blunt et al., 2013](#)]. Information can also be lost during

FIB preparation and cavity milling, or from imaging artefacts caused by the interactions between beam and different-density minerals [Lemmens, H.J. and Butcher, A.R. and Botha, 2011]. Finally, Transmission Electron Microscopy (TEM) provides access to pore connectivity at smaller scales [Gaboreau et al., 2016] but remains limited to 2D slices. 3D reconstruction of the sample at this scale is still particularly delicate and requires electron tomography.

The complexity and sample size limitations when acquiring 3D high-resolution images in comparison with the ease of imaging larger 2D surfaces at high resolution calls for another solution. This alternative consists of using geostatistical methods to reconstruct the pore network from 2D SEM or TEM sections under the same or different orientations. Initially developed for reservoir rock applications, they have been very recently employed on nanoporous materials [Yang et al., 2015, Wu et al., 2018]. Various approaches have been considered for this purpose including Markov Chain of Monte Carlo (MCMC) simulations [Wu et al., 2006, Chen et al., 2015, Tahmasebi et al., 2017a], two-point [Keehm, 2004] or multiple point statistics [Okabe and Blunt, 2007, Hajizadeh et al., 2011, Comunian et al., 2012a, Tahmasebi and Sahimi, 2013, Wu et al., 2018], process-based methods [Øren and Bakke, 2002, 2003], simulated annealing [Ju et al., 2014] or some combination of these methods [Yang et al., 2015, Ju et al., 2017]. The digitalized 3D porous media after reconstruction are then employed in lattice Boltzmann model (LBM), Smooth Particle Hydrodynamics (SPH) or Pore Network Model (PNM) simulations for predicting the transport properties of the material, mainly the intrinsic permeability but also water retention curve, relative permeability and even Klinkenberg effect or Knudsen diffusion for specific applications to nanoporous rocks [e.g., Dymitrowska et al., 2014, Chen et al., 2015, Song et al., 2017, Davy and Adler, 2017, Pazdaniakou et al., 2018, Pazdaniakou and Dymitrowska, 2018, Wei et al., 2019]. If these reconstruction methods are obviously appealing, a new bias appears. The reconstruction of the 3D medium is no longer unique and depends on the interpolation methods used to link the discrete data.

A proper reconstruction giving a fair confidence in the accuracy of effective properties prediction (notwithstanding the uncertainties generated by flow model calculations) needs to be capable of addressing the following questions:

- How to evaluate which reconstruction method(s) is (are) the most suited to capture the effective transport property of interest of the studied sample and how can we evaluate *a priori* the goodness-of-fit of the reconstructed geometries ?
- To which extent the data sparsity is acceptable ? In other words, how many sampling images are required as input for constraining properly the 3D reconstructed domain ?
- And finally what is the impact on transport properties and the uncertainty generated by the reconstruction process?

In this work, we attempt to give a comprehensive overview on these questions. We explore the capability of various stochastic methods to provide a coherent 3D reconstruction of the nanoporous structure of one rock sample from 2D images. Several realisations are performed and the impact of the

distance between two consecutive conditioning data is also discussed. A general framework for analysing the reconstruction methods is proposed based on Minkowski functionals. Since it is well known that permeability tends to average and filter a part of the lower-scale microstructure information, a set of morphological descriptors is used to assess the discrepancy between the original and the reconstructed microstructures. Finally, three transport properties of interest, longitudinal permeability, effective diffusion and longitudinal dispersion are computed and results are discussed.

1 METHODS

For this comparative analysis, we use a stack of FIB-SEM serial-section images of a synthetic clay made from compacted illite powder, which has an overall porosity of 32% [Gaboreau et al., 2016]. The original sample measures 5480x5475x900 nm and was acquired at 5 nm resolution, producing a grid of 1096x1095x180 voxels. A preprocessing treatment has been first applied on RAW FIB-SEM images to remove artifacts. Then, pore space was segmented using a custom-made watershed method as described in Gaboreau et al. [2016]. For computational efficiency, the reconstruction methods were developed and tested on a smaller part of this domain, a regular grid of 180x180x180 voxels (Fig. 1) which is hereafter referred to as the reference 3D image. Note that we do not achieve with this sub-sample the Representative Elementary Volume (REV) of the rock material (the characteristic length of the porosity-based REV is of about 1 μm according to Gaboreau et al. [2016] and it is probably much larger for the other transport property-related REV. However, it does not affect the study results since the computed properties are compared with the ones of the reference 3D image and not with experimental measurements. 2D regularly-sampled parallel slices (xy planes) are then extracted and used as conditioning data for the 3D reconstruction. In the following, we analyse four reconstruction methods and investigate the optimum spacing required between the 2D acquisitions to maintain a correct estimate of hydrodynamic properties. Note that a stochastic approach over a large number of realizations is not applied in the present paper since we do not aim at confronting the predicted transport properties against experimental data.

1.1 Reconstruction Methods

Various methods of 3D reconstructions of the porous medium have been developed in the recent years. They can be classified between two types: object-based and pixel-based methods. A short survey of these methods is detailed below but we refer the reader to the recent review papers of Tahmasebi [2018] or Zhu et al. [2019] for a more comprehensive overview on the advantages and disadvantages of each approach.

Object-based methods directly simulate shapes described by input geometrical, or morphogenetical parameters. Among the object-based methods, pore and throats models, also referred to as pore network models (PNM), are the most common. The pores and throats are respectively assimilated to spheres and cylinders. In early models, these objects were placed following a reconstruction of the sedimentation process [Bakke and Øren, 1997]. In other models, they were randomly placed to reproduce the global porosity [Chen et al., 2015]. The most recent approaches use iterative processes based on genetic al-

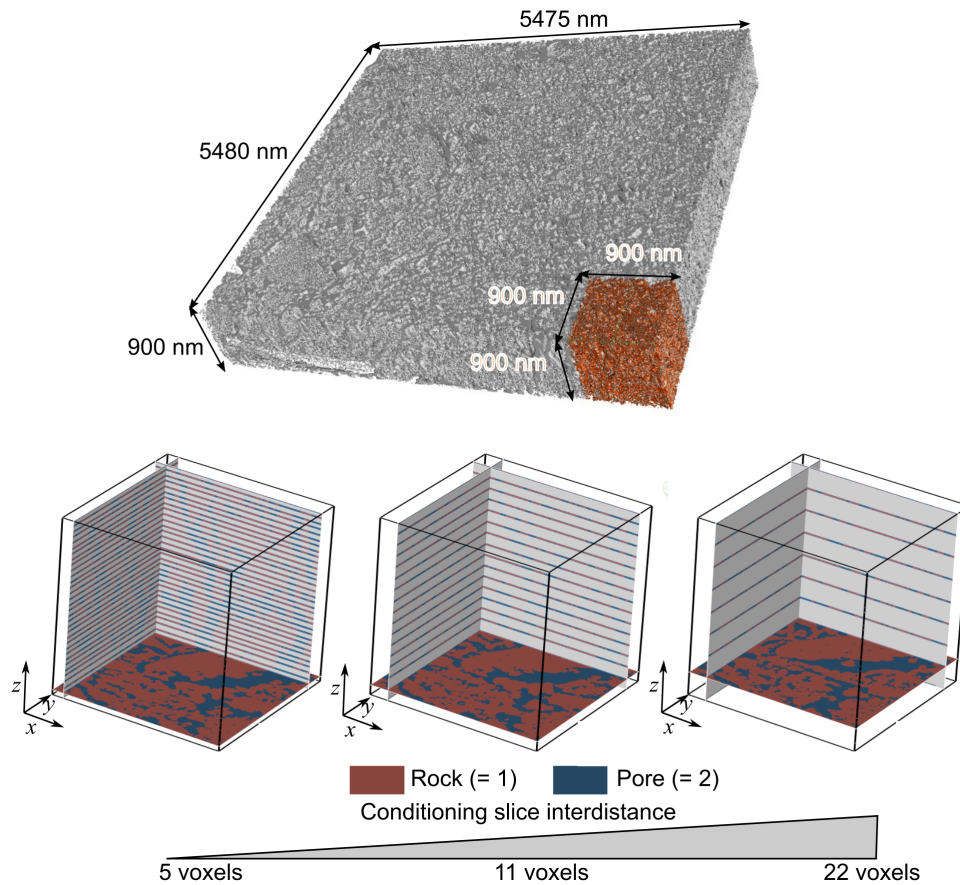


Figure 1 FIB-SEM image of a synthetic clay of 5480x5475x900nm. In red, the reduced domain used for this study (900x900x900nm). Below are represented three input corresponding data cubes (180x180x180 voxels) used for this work: with growing slice inter-distance of 5, 11 and 22 voxels.

gorithms and target porosity and permeability values [Xu et al., 2014].

Pixel-based methods consist in affecting a value to each voxel of a grid. There are three main approaches: i) the Two-Point Statistics types, ii) the Markov Chain Monte Carlo types (MCMC), and iii) the Multiple-Point Statistics (MPS) types. The Two-Point Statistics simulations stochastically set values to voxels in order to reproduce an input property distribution (the histogram) and a spatial covariance (provided by a variogram). The MCMC simulations [e.g. Wu et al., 2006, Tahmasebi et al., 2017a] consist in a progressive filling of the medium according to a pre-determined path and depending on the values of the previously simulated pixels. The porosity of the medium, determined from the analysis of 2D sections, is an input parameter that influences the values affected at each voxel. With several common points with MCMC methods, MPS simulations allow a stochastic reconstitution of a medium based on the analysis of training images that are conceptual models of the simulated media on which high-order statistics can be extracted [Okabe and Blunt, 2007, Comunian et al., 2012a, Chen et al., 2018]. They mainly differ from MCMC by the simulation path which is, in MPS, completely random.

If object-based methods have shown to be able to reproduce media with consistent hydraulic properties, they need a high parametrization, which is not easily compatible with 2D conditioning data, and involves intensive computing [Øren and Bakke, 2002]. On the contrary, pixel-based methods need less parametrization since all the information is computed from the input image data. Flexible and computationally efficient, MCMC methods could be difficult to apply in case of spatially

distributed conditioning data. But Two-Point and Multiple-Point Statistics Simulation are designed to handle conditioning data whatever their location in the domain.

For these reasons, we decided to focus on these two kinds of geostatistical methods to explore their respective ability to consistently reconstruct 3D porous medium from 2D regularly-sampled parallel FIB-SEM slices ((xy) planes) at nanometric scale. For each reconstruction method, three sampling distances between conditioning parallel slices were tested: 5 voxels, 11 voxels and 22 voxels (respectively, 25, 55 and 110 nm).

Sequential Indicator Simulation (SIS)

Sequential Indicator Simulation is the classical Two-Points Statistics simulation method developed for categorical variables [e.g. Journel and Isaaks, 1984, Deutsch and Journel, 1997]. Its simplicity of numerical implementation made it one of the most common geostatistical methods, available in several software. A random path is defined between all voxels. For each selected node, an indicator kriging is performed using the neighbouring subsurface data, previously simulated values, and the global average porosity. The node value is randomly drawn from the resulting local conditional distribution function. This new simulated node is added to the known nodes. This action is repeated until all grid nodes have been simulated.

In this paper, we use the SIS method implemented in the SKUA-Gocad software¹. To carry out the simulation under the same conditions as those set by our application case, we did not compute variograms on the 3D porous medium, but only

¹<http://www.pdgm.com/products/skua-gocad/>

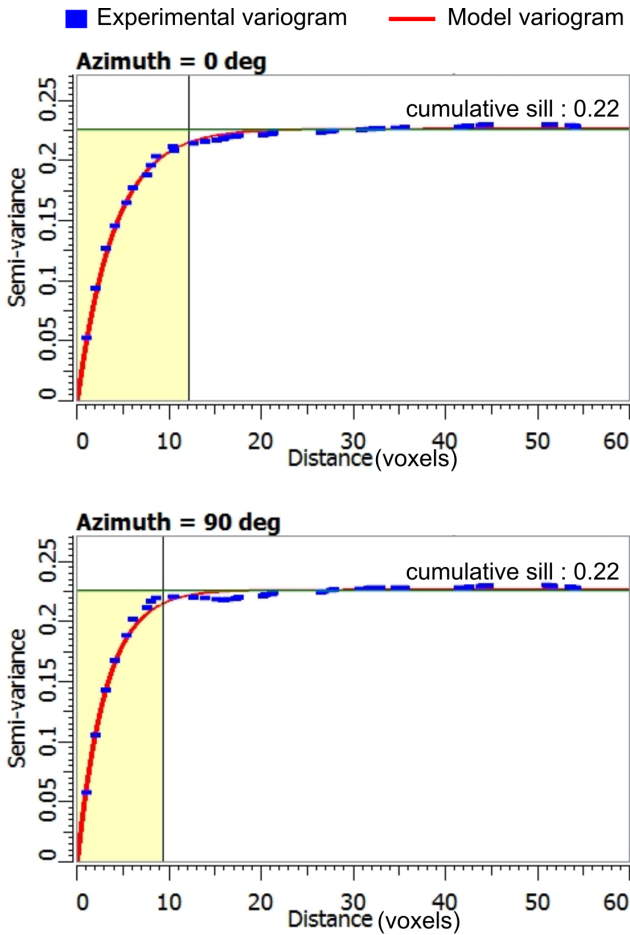


Figure 2 Experimental 2D variogram computed along xy planes from slices spaced by 5 voxels. Here, the corresponding variogram model is Exponential, with no nugget effect, and minimal and maximal ranges of, respectively, 9.1 and 11.8 voxels.

on the spaced conditioning slices, thus on horizontal planes. Similar results (maximal variations of 1 voxel) are obtained for all distances between conditioning slices, i.e., 5, 11 and 22 voxels. The experimental variograms show a slight anisotropy along the horizontal plane (Fig. 2). The used model variogram is an exponential one, with no nugget effect, a sill of 0.226, and with minimal and maximal ranges of, respectively, 9.2 and 12.9 voxels. As no vertical information is considered to be accessible in our case study, the vertical range is arbitrary set to 10 voxels, an average value of the horizontal ranges.

General principles of Multiple Point Simulation (MPS)

The principles of Multiple-Point Statistics have been established by [Guardiano and Srivastava \[1993\]](#). To overcome the limitations of Two-Points Statistics when dealing with complex geometries of connected geological structures, MPS extract the spatial structures from a Training Image (TI), which is a conceptual representation of the modelled medium. Thus, if the TI is anisotropic, the realisations would reproduce this anisotropy [[Strebelle, 2002](#)]. In practice, MPS proceed sequentially. At each successive location, a data event, centered around the simulated point, is extracted from the simulation domain. It regroups the known neighbouring voxels and their relative position around the simulated point. The value assigned to the node is extracted from a cumulative distribution function (CDF), which has been built on the central nodes of TI patterns,

equal or similar to the data event. Several MPS algorithms exist. They differ by the way the CDF is built. For example, the first implementation of MPS, SNESIM [[Strebelle, 2002](#)] proposes to scan the TI and store all the data templates in a tree, while in Impala [[Straubhaar et al., 2011](#)] they are stored in a list. The Direct Sampling algorithm (DS) [[Mariethoz and Renard, 2010](#), [Mariethoz et al., 2010](#)] does not use a CDF, but proposes to go through the training model on a random path, and as soon as the difference between the event in the TI and the data event is inferior to a user-defined threshold, the corresponding central value is set to the simulated node. Quite soon after the initial algorithm of [Strebelle et al. \[2002\]](#) focused on a pixel-by-pixel simulation, an alternative version of MPS has also emerged called pattern-based-MPS [e.g. [Arpat and Caers, 2005](#), [Zhang et al., 2005](#)]. In these methods the simulation processes pattern-by-pattern, like a patchwork reconstruction. Several algorithms exist, with the same hierarchy than for pixel-based-MPS and some recent applications have been made to porous media reconstructions [e.g. [Tahmasebi and Sahimi, 2013](#), [Tahmasebi et al., 2017b](#)]. A complete review can be found in [Tahmasebi \[2018\]](#). In this work, we did not intend to compare all existing methods but provide general guidelines to compare them. We thus decided to focus on one category of MPS, the pixel-based MPS.

In our application case, a main limitation for using classical algorithms of MPS is that we want to reconstruct the porous media in 3D but only from parallel 2D sections. Thus, we do not have a 3D TI at our disposal. Adaptations of MPS have been proposed by several authors [[Okabe and Blunt, 2007](#), [Hajizadeh et al., 2011](#), [Comunian et al., 2012a](#), [Ding et al., 2018](#)]. In all works, 2D TI are required for each orientation, i.e. xy , xz and yz planes. In our case, we consider having only xy plane data. Thus, like [Okabe and Blunt \[2007\]](#), we are going to use xy images also for xz or yz TI. This can be considered as a similar approach to taking an average horizontal range for vertical direction in SIS, and should limit the application to media with reduced anisotropy. For strong anisotropic media, different TIs should be used, one for each orthogonal planes.

We have implemented three derived versions of MPS : i) a new implementation of the three directional aggregation MPS method, 3DA-MPS, proposed by [Okabe and Blunt \[2007\]](#); ii) a slice sequential MPS method, s2Dcd*, inspired by [Comunian et al. \[2012a\]](#); iii) and a modified version of the 3DA-MPS, the weighted-3DA-MPS.

3DA-MPS: a method inspired by the Three Directional aggregation MPS

The principle of the 3DA-MPS is to approximate the 3D conditional probability distribution function by a combination of the probabilities obtained with 2D MPS performed along each direction (Fig. 3). In [Okabe and Blunt \[2007\]](#), the 2D-MPS are performed with the Impala algorithm [[Straubhaar et al., 2011](#)]. To gain in computational efficiency and handle the particular placement of the conditioning data in our application, we implemented 3DA-MPS with the DS algorithm [[Mariethoz and Renard, 2010](#)], which produces the same ensemble of stochastic realisations when used with the same parameters [[Mariethoz et al., 2010](#)]. For each randomly picked simulated node j , three data events (one for each orthogonal direction) are extracted. These data events, $d_n(j)$, are defined by the number n of conditioning data or closest previously simulated voxels in a search radius l , the user-defined size of the template. Each TI (i.e., for

each direction) is then explored starting from a random location, and, as soon as a similar data event $d_n(k)$ is met around the point k (i.e., $d\{d_n(j), d_n(k)\} \leq t$, with t the user-defined threshold value), the value $Z(k)$ at the central point is selected. The distance $d\{d_n(j), d_n(k)\}$ between the data event and the TI event is the proportion of non-matching voxels [Mariethoz and Renard, 2010]:

$$d\{d_n(j), d_n(k)\} = \frac{1}{n} \sum_{i=1}^n m_i, \quad (1)$$

$$\text{where } m_i = \begin{cases} 1 & \text{if } Z(j_i) = Z(k_i), \\ 0 & \text{if } Z(j_i) \neq Z(k_i) \end{cases}$$

The three values (one coming from each direction) are then aggregated to set the final simulated value. Different weighting schemes can be used, and as already stated by Comunian et al. [2012b], this choice has a big impact on the resulting simulations. For the probability aggregation, Okabe and Blunt [2007] use linear pooling formula, while Comunian et al. [2012a] underlined the absence of external Bayesianity property and propose to use Bordley's formula instead. In this work, as the three TI images come from parallel xy sections, there is no reason to prefer one TI over another, and using linear pooling formula is adapted [Comunian et al., 2012a].

However, at the beginning of the simulation, when the data event is almost empty of conditioning data (e.g. in the middle of two distanced slices), for each direction, the probability of setting a *pore* at the simulated node is almost equal to the porosity of the medium, i.e., around 30%. Thus, the probability of having a *pore* value in at least two of the three directional MPS goes down to 11%, and only 3% for having it in the three directional MPS. This point could strongly lead to a minimization of the global porosity, particularly when spacing the conditioning slices. Thus, to reduce this effect, a simulated value is set to *pore*, as soon as one of the three directional MPS set the central value to *pore*.

We use a square 2D template of 9x9 voxels centred on the simulated value (like proposed by Okabe and Blunt [2007]), an acceptance threshold of 0.1 and a maximal number of iterations of 300 for the DS parametrization. The TI used for the presented realizations (Fig. 3) were randomly selected in the available 2D slices, excluding the conditioning data slices.

s2Dcd*: a method inspired by the Sequential bi-dimensional MPS (s2Dcd)

The sequential bi-dimensional MPS simulation and conditioning data (s2Dcd) proposed by Comunian et al. [2012a] differs from the method of Okabe and Blunt [2007] as, instead of randomly selecting nodes in the 3D volume, the media is built slices by slices. The order of simulation of 2D surfaces is not completely random, and, as said by the authors, *should be customized according to the location of the conditioning data and to the shape of the simulation domain* [Comunian et al., 2012a]. They advise to look for orders maximizing the number of conditioning data and alternating the different directions. The MPS are performed on the 2D surfaces using Impala algorithm, but the simulation uses a merged list whose construction is adapted to the particular case of 2D data events combination. This merged list has also the advantage of indicating the 3D compatibility of the 2D TI.

In this paper, we do not intend to propose a generic approach for all geological features at all scales, but we focus only on the reconstruction of 3D porous medium at nanometric scale. Thus, we only have two facies to manage, grains and voids, and our TI - coming from the reference image - should be compatible if the rock does not have a strong anisotropy. Thus, we just implemented a simplified version of the s2Dcd, the s2Dcd*, using Direct Sampling algorithm [Mariethoz and Renard, 2010] instead of Impala, and choosing randomly the slices with alternating directions (Fig. 4). We keep the same DS parameters as in the former 3DA-MPS approach, but uses a unique but larger TI for all directions (Fig. 4).

Weighted Three Directional aggregation MPS (weighted-3DA-MPS)

A third class of the 3DA-MPS was implemented motivated by the idea to limit the porosity minimization effect of the combination of three independent simulated values along the 2D planes. It consists in modifying the way the distance $d\{d_n(j), d_n(k)\}$ between the data event, $d_n(j)$, and the configurations found in the TI, $d_n(k)$, are compared. In the previous methods, the distance is simply equal to the proportion of non-matching voxels, as initially proposed by Mariethoz and Renard [2010]. In weighted-3DA-MPS implementation, the distance $d\{d_n(j), d_n(k)\}$ is a function of the porosity ϕ :

$$d\{d_n(j), d_n(k)\} = \sum_{i=1}^n \frac{m_i}{c_i}, \quad (2)$$

$$\text{where } m_i = \begin{cases} 1 - \phi & \text{if } Z(j_i) = Z(k_i) = \text{pore}, \\ \phi & \text{if } Z(j_i) = Z(k_i) = \text{rock}, \\ 0 & \text{if } Z(j_i) \neq Z(k_i) \end{cases}$$

$$\text{and } c_i = \begin{cases} m_i & \text{if } Z(j_i) = Z(k_i), \\ \phi & \text{if } Z(j_i) \neq Z(k_i) \end{cases}$$

With this implementation, not only the number of absolute voxel mismatches counts, but also the porosity of the observed TI events. For an equal number of non-equal voxel values, if $\phi \leq 50\%$ the TI event with the highest porosity will be preferred (if $\phi > 50\%$ it would be the lowest one).

In the application, we used $\phi = 30\%$ which corresponds to the average porosity computed on the used TI images (Fig. 3).

1.2 Post-processing

When performing reconstruction processes, regardless how successful the pore space is digitalized, some artifacts are generated which may affect computation of transport properties [Ortega Ramírez et al., 2019, Pot et al., 2020]. They result both from image acquisition (cavity milling, etc.), image segmentation (loss of pores during identification) or from the reconstruction method itself and need to be managed. These artifacts are manifested in different ways, including curtaining effect, disconnected pores or intensity variation and an appropriate advanced image processing has to be applied to mitigate them [Salzer et al., 2015, Zhu et al., 2019]. For instance, isolated pores or solid voxels are often generated when using MPS approaches, and even more with SIS. Part of the difficulty is that each artifact requires a specific image filtering method, namely noise reduction, sharpening, shading correction and FFT- or median- filtering. But such a digital processing may

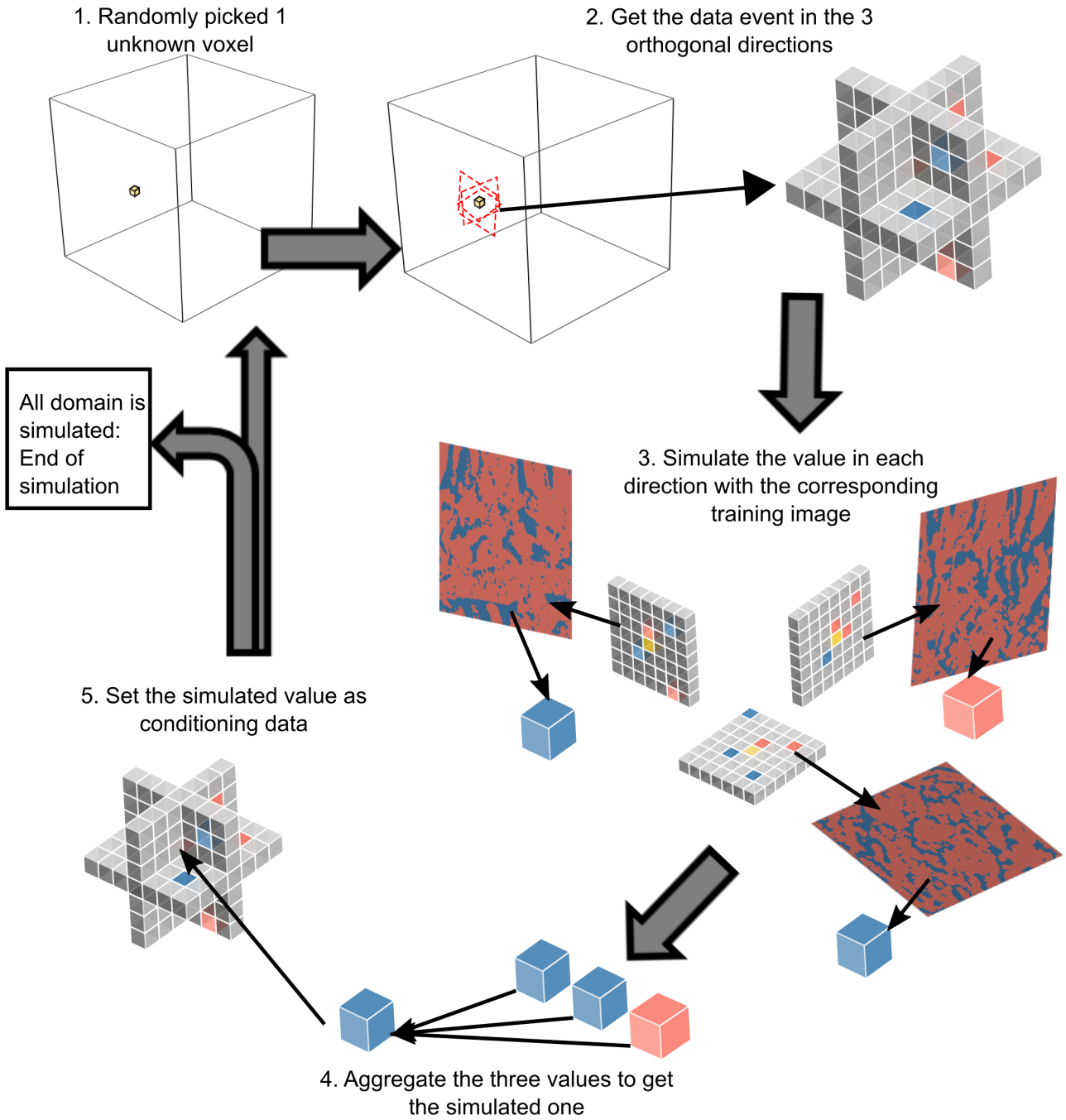


Figure 3 Principle of the 3DA-MPS method. This method is inspired by [Okabe and Blunt \[2007\]](#) but differs as MPS are realized using DS algorithm [[Mariethoz et al., 2010](#)] instead of Impala [[Straubhaar et al., 2011](#)].

also significantly modify the original image and hence alter the related transport properties [[Gunda et al., 2011](#)].

Hereafter, we chose to apply the same morphological post-processing steps to all the 3D volumes, independently of the reconstruction method used. The image processing could be probably optimized by selecting the most appropriate filtering methods for each realization but it would also skew our comparative analysis. As a consequence, we removed first the non-connected porosity and then we applied an opening of 1 voxel to suppress the isolated solid voxels. In order to assess the impact of this post-processing step, it was also applied to the reference image and will be later labelled as 'post-processed'. A comparison of alternative solutions of filtering (including without postprocessing) is investigated in a second step.

1.3 Image Analysis

In order to compare reconstructed images to the reference image, and therefore to assess the performance of the reconstruction methods, different morphological descriptors are selected. [Armstrong et al. \[2019\]](#) provided a review and prospects of the use of Minkowski functionals for characterization of porous media, especially regarding single-phase and multi-phase flow properties. For instance, intrinsic permeability is classically related to the porosity (for instance using Kozeny-Carman equation), but may also be linked to the Euler characteristic [[Scholz et al., 2012](#)].

In the present study, three Minkowski functionals are used in regards to the pore structure: the first functional computes the pore volume and thus the porosity (ϕ), the second functional allows calculation of the specific surface (S_v) and the fourth

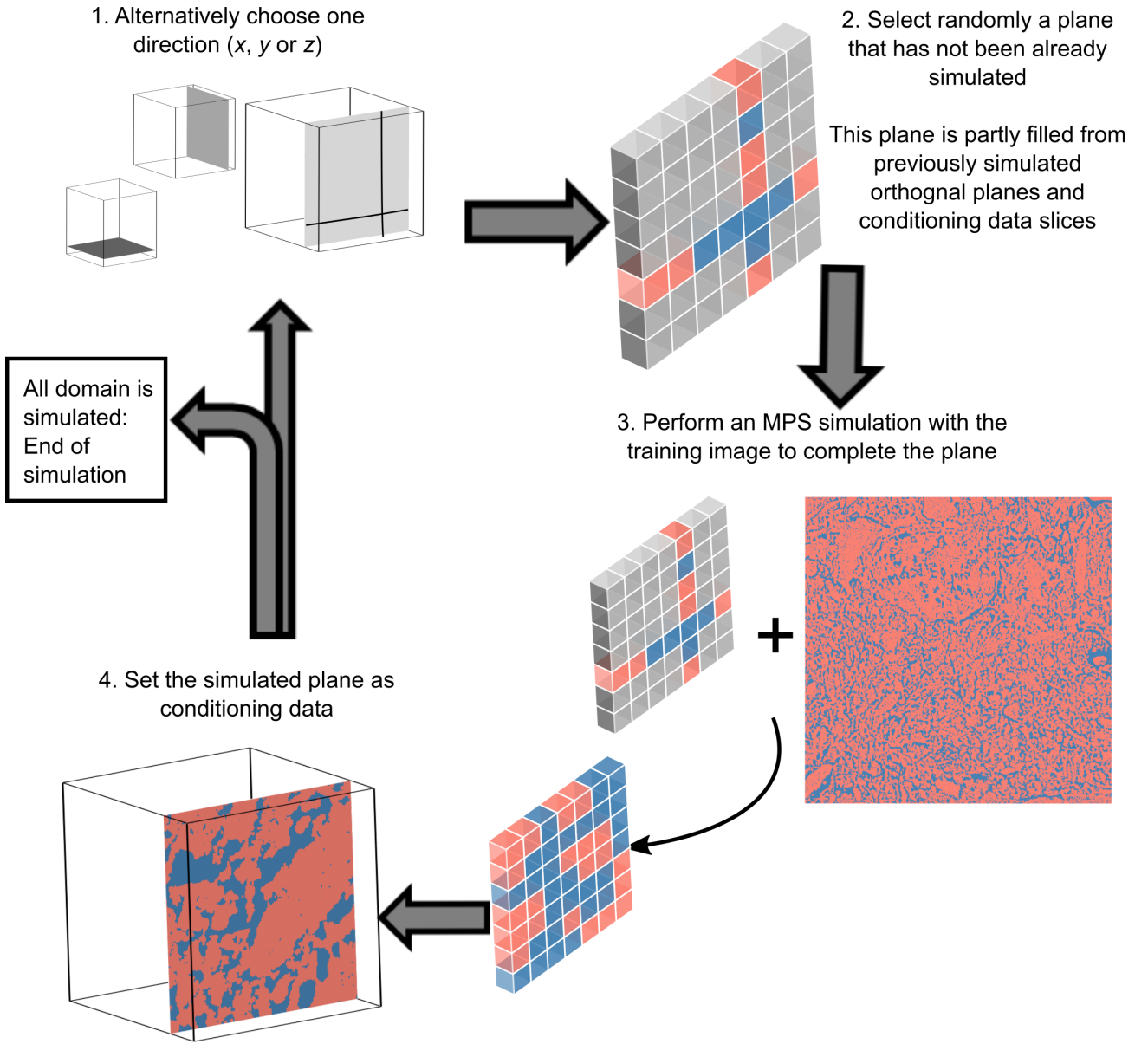


Figure 4 Principle of the slice sequential MPS method (s2Dcd, inspired by [Comunian et al. \[2012a\]](#)) implemented in this work

functional corresponds to the Euler characteristic (χ). The latter may also be computed from the Betti numbers (isolated pores, loops and isolated solids, in the present context). Porosity, specific surface and Euler characteristic were computed using the ImageJ plug-in MorpholibJ [[Legland et al., 2016](#)].

The tortuosity is calculated as the ratio of the smallest geodesic distance (shortest distance between two points within a given phase) to the euclidian distance between the inlet face and the outlet face in the z-direction. The geodesic distance is computed by a series of dilations and intersections following the methodology described in [Gommes et al. \[2009\]](#) and the euclidian distance corresponds to the size of the sample.

The pore size distribution (PSD) is computed using the ImageJ plug-in XLib [[Münch and Holzer, 2008](#)] following the continuous PSD approach on the 3D images.

1.4 Numerical Upscaling

The computed intrinsic permeability (later referred as intrinsic permeability) is computed using numerical upscaling. The Navier-Stokes equation for flow in the pore structure is solved

using a Lattice Boltzmann approach. The Lattice Boltzmann methods represent the fluid as fictive particles that undergo collision and propagation processes and lead to the calculation of 'particle density' ρ and velocity field (u_x, u_y, u_z).

In the present study, a D3Q19 TRT LBM approach was used with bounce-back fluid-solid boundaries [[Ginzburg et al., 2008](#), [Pazdniakou and Dymitrowska, 2018](#)]. More details on the model may be found in [Pazdniakou and Dymitrowska \[2018\]](#). The original image was mirrored in the z-direction and padded with walls on the lateral sides in order for periodic boundary conditions to be used. Flow in the porous system was modeled by a force F along the z-direction [[Pan et al., 2006](#)]. The intrinsic permeability (m^2) is computed from the density and velocity fields following eq. (3).

$$K_{zz} = \frac{\delta^2 \nu \sum (\rho u_z)}{VF} \quad (3)$$

Where δ is the image resolution (5 nm), ν is the viscosity in lattice units ($= 1/6$), V is the number of voxels in the mirrored image, F ($= 10^{-7}$) is the imposed force in lattice units and ρ and u_z are the density and velocity in z-direction fields

respectively.

The computed effective diffusion and computed dispersion (later referred as effective diffusion and dispersion respectively) are computed using numerical upscaling. The advection-diffusion transport equation is solved using a D3Q7 LBM following Yang and Chu [2013]. The LBM methods thus allow the computation of the concentration field. For the dispersion simulations, the velocity field used is the one calculated from the flow equation normalized to reach an average z-velocity of 0.005 in lattice units, leading to an average local Peclet of 3.3. Similarly to Yang and Chu [2013], the transport is solved from an initial pulse, considering periodic boundaries on all sides. The initial pulse is set at $z = 90$ voxels and the simulation is computed at least until the pulse spreads over 180 voxels, corresponding to the original image size. The method of moments [Garabedian et al., 1991] is then applied as a post-processing step in order to compute the effective diffusion and dispersion for a given imposed diffusion parameter (0.05 for the effective diffusion calculation and 0.002 for the dispersion calculation) (eq. (4)) as well as the mean displacement rate (eq. (5)).

$$D_{zz} = \frac{\partial}{\partial t} \iiint \frac{(z - \bar{z})^2}{2M_0} C dx dy dz \quad (4)$$

$$\bar{u}_z = \frac{\partial \bar{z}}{\partial t} = \frac{\partial}{\partial t} \iiint \frac{z}{M_0} C dx dy dz \quad (5)$$

Where \bar{z} is the mean displacement of the solute and $M_0 = \iiint C dx dy dz$ is the total solute injected in the system. The effective diffusion and the dispersion computed are normalized against the imposed diffusion parameter.

2 RESULTS AND DISCUSSION

The four reconstruction models (Sequential indicator simulation (SIS), Slice sequential MPS (s2Dcd*), Three directional aggregation MPS (3DA-MPS), Weighted three directional aggregation MPS (weighted-3DA-MPS)) are applied to the reference image data, considering training images with average porosity of 30% for the MPS approaches (see Fig.3 and Fig.4). The conditioning slices are normal to the z-direction and spaced by 5, 11 or 22 voxels (Fig.1). For each case, five realizations were performed. Morphological parameters (porosity, specific surface, Euler characteristic, tortuosity and pore size distributions) are computed and compared to the reference image properties. Then, effective transport properties (permeability, effective diffusion and dispersion) for a given realization of each reconstruction approach and for each distance between conditioning data are compared. Finally, the impact of the post-processing is assessed.

2.1 Reference Data

The reference image (Fig. 5) has a porosity of 34.4% with over 98% of the porosity interconnected and percolating, and a specific surface of $113.5 \mu m^{-1}$. Its Euler characteristic is of -2392.5 reflecting its connected pore structure. The tortuosity of the reference image is quite low at a value of 1.05. The pore size distribution of the reference image (Fig.8) is rather uniformly graded between diameter 5 nm and 60 nm for the most part ($D_{50} = 33 \text{ nm}$, $D_{10} = 15 \text{ nm}$ and $D_{90} = 58 \text{ nm}$). The permeability of the sample along the z-axis is of $4 \times 10^{-18} m^2$,

the effective diffusion and longitudinal dispersion, normalized against input diffusion, are respectively of 0.43 and 12.4.

In the reference image (Fig. 5), larger solid structure with included porosity can be observed. It should be noted that the post-processing removes such included porosity. The pores appear to be orientated preferably in the z-direction, reflecting the anisotropy that could be observed when performing a 3D-variogram (vertical range of 14 voxels). It should be noted that the medium was compacted in the x-axis direction.

2.2 Direct Observation

Images of the first realization for each reconstruction approach and each distance between conditioning data are shown in Fig. 6.

The 3DA-MPS approach demonstrates a little of curtain-like noise but allows good description of the larger grains. In other words, solid voxels planes or lines appear in a pore volume or inversely (Fig. 6, zoomed areas). The pores elongation in the z-direction is well recovered for a distance of 5 voxels between conditioning data, though this behaviour is diminished when the distance increases. Indeed, at 22 voxels distance, the pores have seemingly a more sphere-like shape.

The s2Dcd* and weighted-3DA-MPS approaches demonstrate heavier curtain-like noise, even after post-processing. The larger solid grains are well described, albeit tend to disappear with less conditioning data, especially for the weighted-3DA-MPS approach. Similarly to the 3DA-MPS method, the pore elongations in the z-direction can be observed with high conditioning and tend to decrease when the distance between conditioning data increases. The weighted-3DA-MPS approach appears to maintain the pore shapes better than the s2Dcd* reconstruction in low conditioning cases. For all MPS-based method, the loss of vertical continuity of pore shapes observed for 22 voxels-spaced simulations is certainly linked to the chosen search radius size. Indeed, a template size of $9 \times 9 \times 9$ voxels allows simulations to start with almost always conditioning data in the data event for 5 and 11-voxel spaced cases (in this last case, only the points located exactly in the middle of two conditioning slices are not constrained at the beginning of the simulation). But with a 22-voxel spaced slices, almost 50% of the simulated points have empty data events at the beginning of the simulation, favouring random (mis-)connections of two consecutive slices. Using a higher search radius should certainly improve the results.

The SIS realizations do not show curtain-like noise, but are fuzzier than MPS reconstructions. Larger grains tend to be filled with connected porosity, especially when the amount of conditioning data diminishes. The pore elongations are barely observable from a distance of 11 voxels, which is consistent with the input vertical range of 10 voxels. Using a higher vertical range should increase the pore elongation, but supposes the anisotropy of the media is known at the beginning.

2.3 Morphological Comparison

Variations of morphological parameters - porosity, specific surface, Euler characteristic and tortuosity - compared to the reference sample are shown for each reconstructed approach in Fig. 7. The variations of the morphological parameters in between realizations remain reasonable, even with limited conditioning data, and are significantly lower than the discrepancy between the various reconstruction methods. It supports the fact

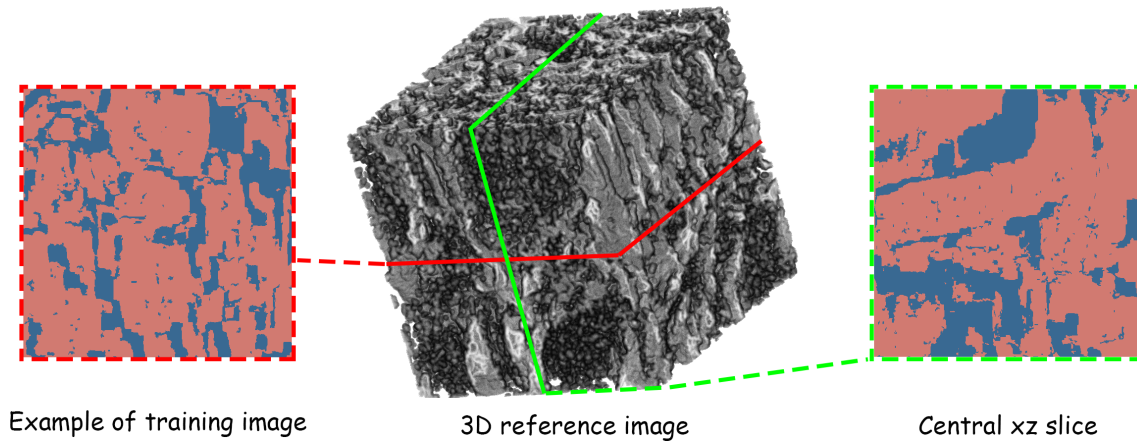


Figure 5 3D reference image, cross section view along the central xz plane and an example of training image used in the reconstruction methods.

that the gap between methods can be investigated based on this comparative analysis. The post-processed reference image demonstrates an increase in porosity of 7%, of the Euler characteristic of 60%, a decrease in specific surface of 18% and maintains the tortuosity. The post-processed reference PSD translates the reference PSD by roughly 5 nm (1 voxel) (Fig. 8), therefore leading to larger pore size.

The SIS approach shows higher porosity than the reference (Fig. 7). Considering that the SIS fits inherently the input porosity provided by the histogram from conditioning slices, this higher value is due to the post-processing. The Euler characteristic is also significantly higher than the one of the reference sample which indicates more loops within the pore volume and may be linked to the fuzziness observed on the images. The specific surface and tortuosity are well described. For the SIS approach, the error for porosity and tortuosity compared to the reference increases when distance between conditioning data increases, whilst no specific trends can be determined for specific surface and Euler characteristic. The PSD (Fig. 8) of the SIS reconstructed with a distance of 5 voxels superimposes the PSD of the reference data. When the distance between conditioning data increases, however, the SIS tends to homogenize the pore sizes even further, reducing the amount of larger pores.

The 3DA-MPS shows very similar behaviour for distance 5 and 11 voxels (Fig. 7), with good description of porosity and tortuosity, underestimation by about 30% of the specific surface and by about 40% of the Euler characteristic. At a distance of 22 voxels between conditioning data, the morphological parameters significantly differ with a loss in porosity of about half, a large increase in tortuosity and a further increase of the Euler characteristic error. The specific surface is, however, improved. The 3DA-MPS approach leads to larger pores compared to both the reference and the post-processed reference. At the largest distance, however, the PSD of the 3DA-MPS reconstruction (Fig. 8) is very similar to the one of the post-processed sample, except for larger pores. It should be noted that the evolution of specific surface and PSD, for 3DA-MPS, is similar. The 3DA-MPS images with smaller conditioning distance lead to good representation of the larger pores, as observed in the previous section, yet the interface details, with smaller characteristic length, are not as well represented, especially due to the post-processing. Therefore, the specific surface is significantly lower and the PSD tends to favor medium size pores over smaller size

pores.

The s2Dcd* reconstructions demonstrate clear correlations with the amount of conditioning data (Fig. 7). Indeed, the porosity and Euler characteristics decrease with increasing distance and conversely, specific surface and tortuosity increase. In regards to the error between realizations and the reference sample, there is a steady increase of this error for porosity and tortuosity. The s2Dcd* PSD (Fig. 8) is very close to the post-processed reference at a distance of 5 voxels, with a diminution of the pore size of roughly 1 voxel with increasing distance between conditioning data.

The weighted-3DA-MPS approach provides consistent morphological characteristics with the reference sample, even with little conditioning (Fig. 7). At a conditioning distance of 5 voxels, the weighted-3DA-MPS reconstruction is, however, closer to the post-processed sample than to the reference sample. At a larger distance, the porosity diminishes slightly and the tortuosity increases, albeit much less than the ones from s2Dcd* and 3DA-MPS realizations. Similarly to the s2Dcd*, the weighted-3DA-MPS PSD (Fig. 8) is close to the post-processed PSD with high amount of conditioning data. However, pore sizes seemingly increases by about 1 voxel for lesser conditioning. It should also be noted that the variation of the PSD between realizations is more important for the weighted-3DA-MPS approach than for the other methods, especially with little conditioning.

2.4 Effective Properties

Given the very low variability over realizations of these various morphological parameters, comparative analysis of effective properties is conducted hereafter for a single realization of each reconstruction method but for different spacings between conditioning data. Quantifying the uncertainty in transport properties would require to perform simulations over a large ensemble of stochastic realizations and will not be addressed here. Variations of effective properties, namely the permeability, effective diffusion and dispersion, are provided in Fig. 9. First, we observe that the post-processed sample shows a higher permeability and effective diffusion than the reference sample, likely linked with the increase in pore size diameter and subsequent increase in porosity. The dispersion is, however, lowered by about 30% compared to the reference value.

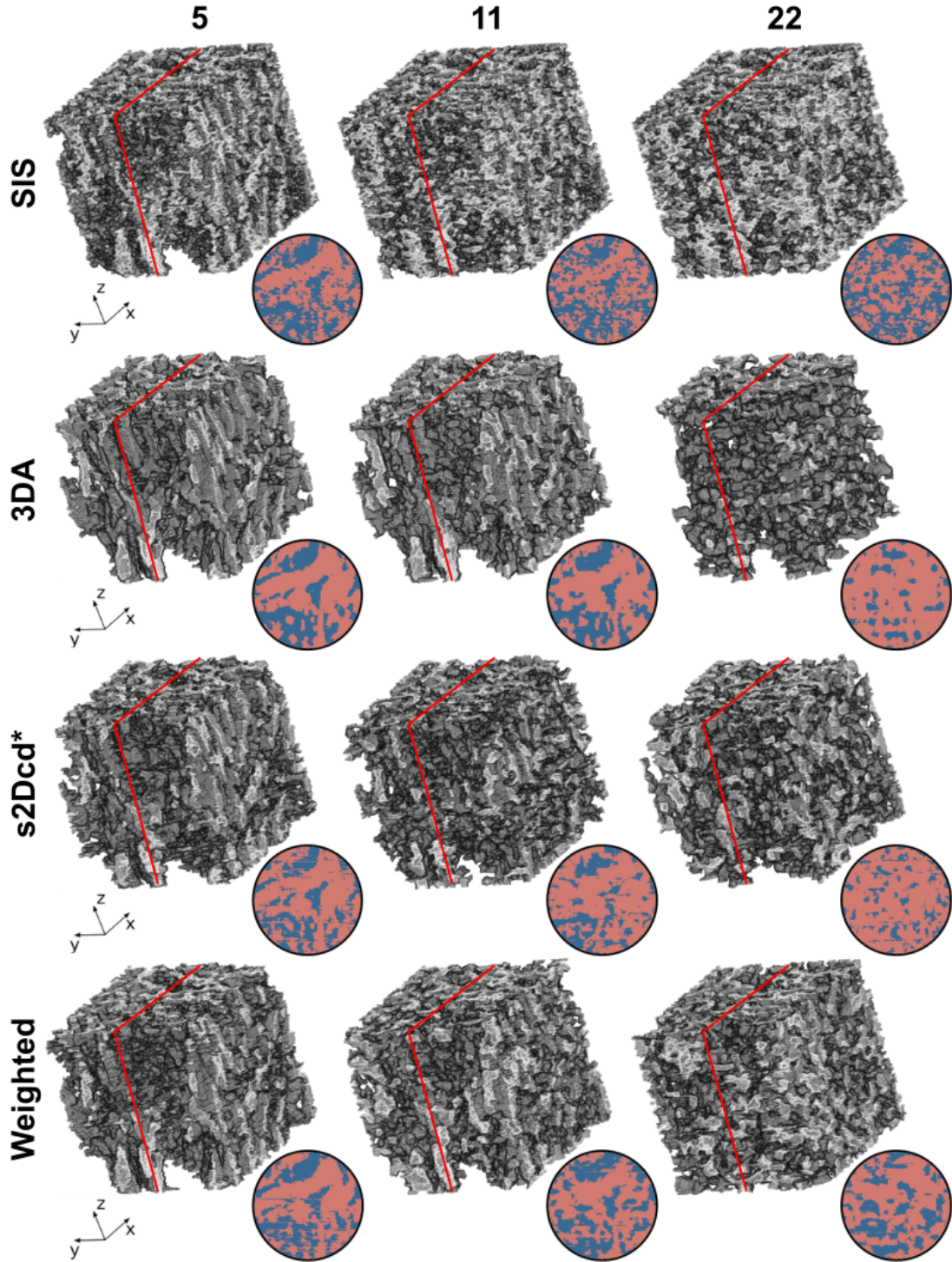


Figure 6 3D images of the first realizations, after post-processing, for each reconstruction approach and each distance between conditioning data. Circle at the bottom right of each 3D image show an extract of the central xz slice. 3DA and Weighted correspond, respectively, to the 3DA-MPS and weighted-3DA-MPS methods.

As stated in Section 1.4, the dispersion computations were performed for a local average Peclet of 3.3 considering the median pore size as characteristic length. But for some realizations (s2Dcd* and 3DA-MPS with 22 voxels distance), the ratio between maximum velocity and average velocity in the z -direction was too important, leading to significantly locally higher Peclet, and thus to divergence of the transport simulation. The acceptable ratio is roughly below 30, leading to the limit Peclet of 100 stated in Yang and Chu [2013].

It should be noted that, aside from s2Dcd* and 3DA-MPS

realizations at the largest distance between conditioning data, the permeability, effective diffusion and dispersion for all methods remains within the same order of magnitude.

The SIS approach shows a steady decrease of the permeability and effective diffusion with the increase of the distance between conditioning data, despite an increase in porosity. For the permeability, this behaviour is explained by both the decrease in pore size and the increase in tortuosity. The MPS methods, except for the weighted-3DA-MPS -11 case, demonstrate a decrease in permeability and effective diffusion when

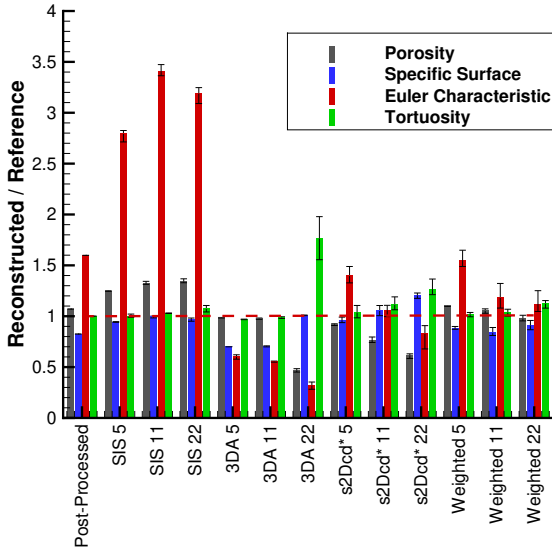


Figure 7 Ratio of a morphological characteristic averaged on all realisations for the reconstructed images to the reference. Post-processed corresponds to the reference image when the post-processing is applied. Error bars indicate variations in between realizations.

the amount of conditioning data is decreasing. This is consistent with the increase of porosity and of tortuosity observed on the realizations. The permeability of the weighted-3DA-MPS approach for 5 and 11 voxels distance and SIS-11 shows good agreement with the reference while the 3DA-5, 3DA-11 and SIS-5 have better agreement with the post-processed reference data. All these six cases demonstrate good agreement with the reference data for effective diffusion. The s2Dcd* and the 22 voxels distance realizations underestimate, however, the permeability and the effective diffusion more significantly. This is coherent with the lower porosity and the larger tortuosity of these reconstructions. The evolution of permeability with conditioning distance cannot, however, be only correlated to the porosity and tortuosity. Indeed, these morphological properties show little variation for the weighted-3DA-MPS, and the evolution of permeability does not follow the trend defined by the Euler characteristic either. Therefore, it is likely that other morphological properties would be required to properly explain the permeability variation with conditioning distance. It should be noted that the underestimation of specific surface and discrepancy in the PSD observed for 3DA-5 and 3DA-11 do not seem to significantly influence the computed effective properties.

In order to further illustrate the transport, and therefore the dispersion, the normalized velocity fields and the normalized concentration at a given time are shown in Fig. 10-11.

The reference sample demonstrates preferential pathways (Fig. 10). This leads to a very inhomogeneous distribution of concentration with finger-like progress of the concentration front along the preferential pathways (Fig. 11). Such a behaviour is observed in 3DA-5, 3DA-11 and, to a lesser extent, in the weighted-3DA-MPS realizations. Consequently, these cases have a dispersion close to the reference. The flow pattern for 3DA-22, s2Dcd*-11 and s2Dcd*-22 differs significantly from the other MPS simulations (Fig. 10). Indeed, the flow seems more 'structured', with pores generated around the conditioning data, mostly normal to the z -direction and smaller

links joining the conditioning slices. Such patterns explain the larger tortuosities. Despite this, the s2Dcd*-5 and s2Dcd*-11 realizations still maintain preferential flow in z -direction, albeit less than the reference samples.

The velocity field of the SIS reconstructions are more homogeneous, leading to a more horizontally spread concentration front, and therefore to a smaller dispersion.

2.5 Impact of post-processing

It is interesting to note that the effective properties of 3DA-5 and SIS-5 resemble more those of the post-processed reference than those of the reference. On top of that, as stated previously, curtain-like noise is still significant in the s2Dcd* and weighted-3DA-MPS realizations. Therefore, it is important to assess the impact of post-processing, if any, on the morphological and effective properties. To this end, these properties were computed on 3DA-5, 3DA-11 and SIS-5 where no post-processing was applied and on weighted-3DA-MPS -5, weighted-3DA-MPS -11 and s2Dcd*-5 where a median filter was applied as post-processing. The median was a 3D filter with 2 voxels radius. If the result of the median filter led to an uncertain value of the voxel (i.e. the voxel has the same amount of neighbouring solid and pore voxel), the voxel was considered as a pore voxel. Fig. 12 illustrates the impact of the post-processing (or lack of) on a given image. On the no-filter images, the isolated voxels (pore and solid) generated with the weighted-3DA-MPS approach can be easily spotted. The initial post-processing effectively removes such features while the median filter further smooths the pore and solid interfaces.

Removing the post-processing led to a loss of porosity (which was increased by the post-processing) and an increase in specific surface (due to non-connected porosity). The lower porosity might be due to the fact that the TI average porosity is lower than the reference porosity. Despite the loss in porosity, the 3DA-MPS realizations without post-processing showed good agreement with the reference, both in regards to morphological and transport properties. This is especially true at 5 voxels distance between conditioning data where the realization properties are almost identical to the reference. For the SIS realization, however, the lack of post-processing did not lead to improvement. Indeed, the error for specific surface, but also for effective diffusion remains, and the dispersion could not be computed. The permeability for the SIS sample is significantly lower than the post-processed one, yet the discrepancy with the reference value remains similar.

Median filtering provides much better removal of the curtain-like noise compared to the initially chosen post-processing. In regards to morphological properties, median filtering led to a decrease in porosity, specific surface, and, to a lesser extent, of the tortuosity (Fig. 13). The pore size distribution is, however, mostly translated towards larger pores by 1 to 1.5 voxels, with smaller size pores disappearing. The effective diffusivities (Fig. 14) are increasing despite the loss in porosity. Permeability increases for the weighted-3DA-MPS 5 voxels, decreases for the weighted-3DA-MPS 11 voxels and is maintained for the s2Dcd* filtered realizations. Dispersion is increased for both weighted-3DA-MPS simulations. Unlike in the previous post-processing, dispersion computation could be performed for the s2Dcd*-5 reconstruction and shows significant overestimation compared to the reference.

Overall, whilst the prediction of morphological properties - porosity and specific surface - were degraded compared to the

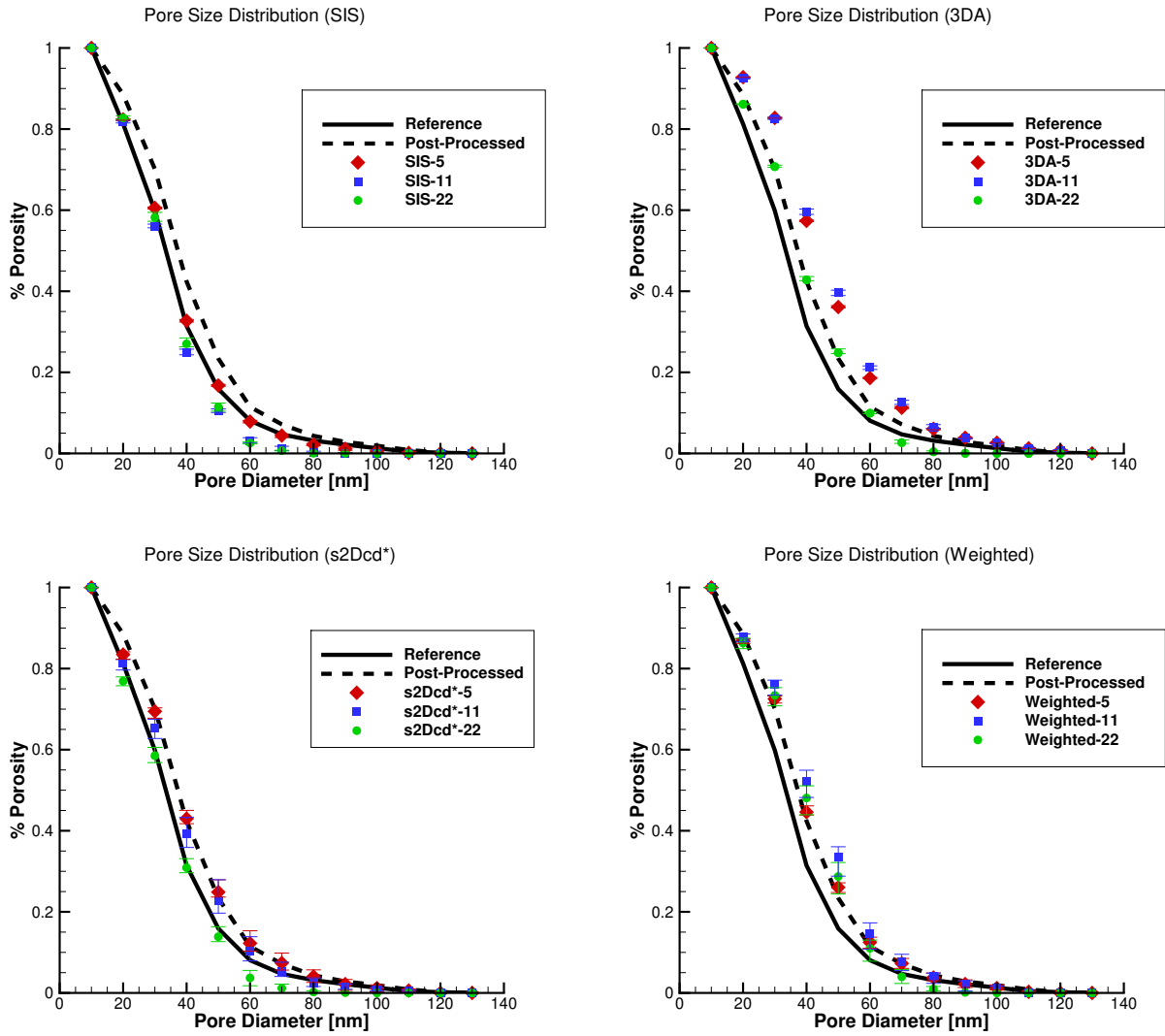


Figure 8 Pore Size Distribution (PSD) for the different approaches. Post-processed corresponds to the reference image when the post-processing is applied. Error bars indicate variations in between realizations.

previous post-processing and even though the change of filter leads to modification of the effective properties, there is no evident improvement or degradation of the transport properties with median filtering. Moreover, the general behaviour of the reconstructed samples for each method remains similar to the one using the initial post-processing, with the weighted-3DA-MPS realizations showing relatively good agreement with the reference and the s2Dcd*-5 realization being less accurate.

3 CONCLUSION

In this study we investigated the capability of different pixel-based methods to reconstruct a coherent 3D nanopore space of clay rock from parallel 2D images as we could obtain from FIB-SEM or TEM imaging. The studied media was almost isotropic and the different methods we used would have to be adapted in the case of a strong anisotropic media, notably by i) choosing dedicated TIs for each orthogonal directions and ii) eventually adapting the template size, which should be bigger in the main anisotropy direction.

The aim was not to make an exhaustive comparison of all existing reconstruction methods, not to find an universal best

one, but to propose, based on a real sample study, general guidelines i) to choose the most appropriate method and ii) to identify the accurate sampling distance when dealing with spaced parallel cross-sections.

Because a direct 3D comparison does not reflect the relevance of the methods, we also analysed the amount of morphological features that was preserved. This is achieved by comparing Minkowski functionals, namely pore volume, specific surface and Euler characteristic as well as tortuosity and PSD. Given the low variability of these various morphological criteria over realizations, we assessed how these 3D reconstructions honour the transport properties of interest from a given realization and we discussed how the sampling distance should be chosen according to the nature of the properties at stake.

From the results described in this work, the following conclusions can be put forward:

- The SIS approach reveals a good agreement of averaged properties but also a lack of description of preferential patterns as indicated by the observed discrepancy for the Euler characteristic and hence for the predicted dispersion coefficient.
- In addition to exhibiting artefacts, the relevance of

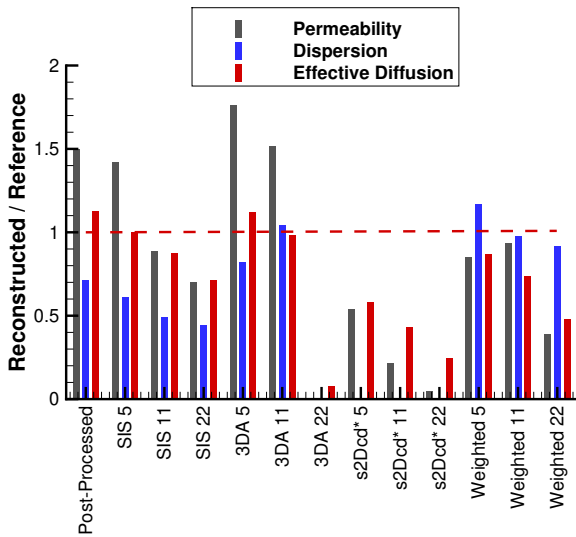


Figure 9 Ratio of effective properties for one realisation of the reconstructed images to the reference. Post-processed corresponds to the reference image when the post-processing is applied.

s2Dcd* approach is highly dependent on the amount of conditioning data. The image reconstruction is satisfying with high conditioning but quickly degrades. According to [Comunian et al. \[2012a\]](#), the path of reconstruction is crucial. It is very likely that an improvement of the path would lead to better results.

- On the contrary, the 3DA-MPS approach exhibits very good results for all the transport properties when the density of conditioning data is large but with no post-processing required. When the distance between conditioning data is close to the characteristic length (as obtained from the variogram), the reconstruction remains acceptable, but degrades strongly afterwards.
- Finally, the weighted-3DA-MPS approach shows better consistency with decreasing conditioning data, but leads to noise in the reconstructed images and is not as accurate at high conditioning as 3DA-MPS. It calls for more advanced weighting and post-processing steps.
- Permeability and effective diffusion were shown to be strongly related to morphological parameters such as porosity and tortuosity. No evident correlation between dispersion and the measured morphological properties was however put forward. This calls for other morphological characterisation to fully assess the acceptability of a given realisation in regards to this transport process. Indeed, dispersion further discriminates the reconstruction approach in comparison to permeability and effective diffusion.
- Concerning the sampling distance, it is clear that choosing a spacing inferior to the vertical range of correlation (in our case, 14 voxels) clearly facilitates a satisfying 3D reconstruction. In practice, this also supposes to be capable of estimating this range, and thus of performing a variogram analysis in the orthogonal direction to the further sampling. This upper limit of sampling distance

is particularly critical for SIS but MPS-based methods could be less impacted since increasing the maximum search distance would partially mitigate this. In a more comprehensive way, this is a severe disadvantage for application to nanoporous rocks which exhibit a large pore size distribution and multi-scale features with different correlation lengths. Here, we face a classical drawback of MPS methods, which are found to be good in conditioning the point data but fail to reproduce long-distance connectivity [[Tahmasebi, 2018](#)].

As a conclusion, this study provides a general guideline for deciding which method will predict the best 3D reconstruction results depending on the amount of 2D images available and the transport property targeted for prediction. These findings are, however, valuable for the specific conditions we used, and, as previously said, the studied media was almost isotropic. MPS-based methods imply various parameters, among them the choice of the TI, the search radius size, and, in this specific application, the value-aggregation method (for 3DA-MPS methods), and the similarity computation between events. All these parameters strongly impact the results and a sensitivity analysis implying all these aspects could be performed to refine the recommendations on the most suitable reconstruction method. Our comparative analysis could also be extended to more recent algorithms. For example, a hybrid approach combining MPS method with object-based or pattern-based method as proposed by [Tahmasebi \[2017\]](#) could certainly be a research route for future improvements, as well as the ones combining the forces of MPS and deep-learning [[Kamrava et al., 2019](#)]. It should be also kept in mind that determining the most suited reconstruction method for predicting the effective property of interest does not prevent from quantifying the uncertainties. An ensemble of stochastic realizations would be ultimately required to estimate the distribution of transport property and the averaged value for DRP application to real porous media.

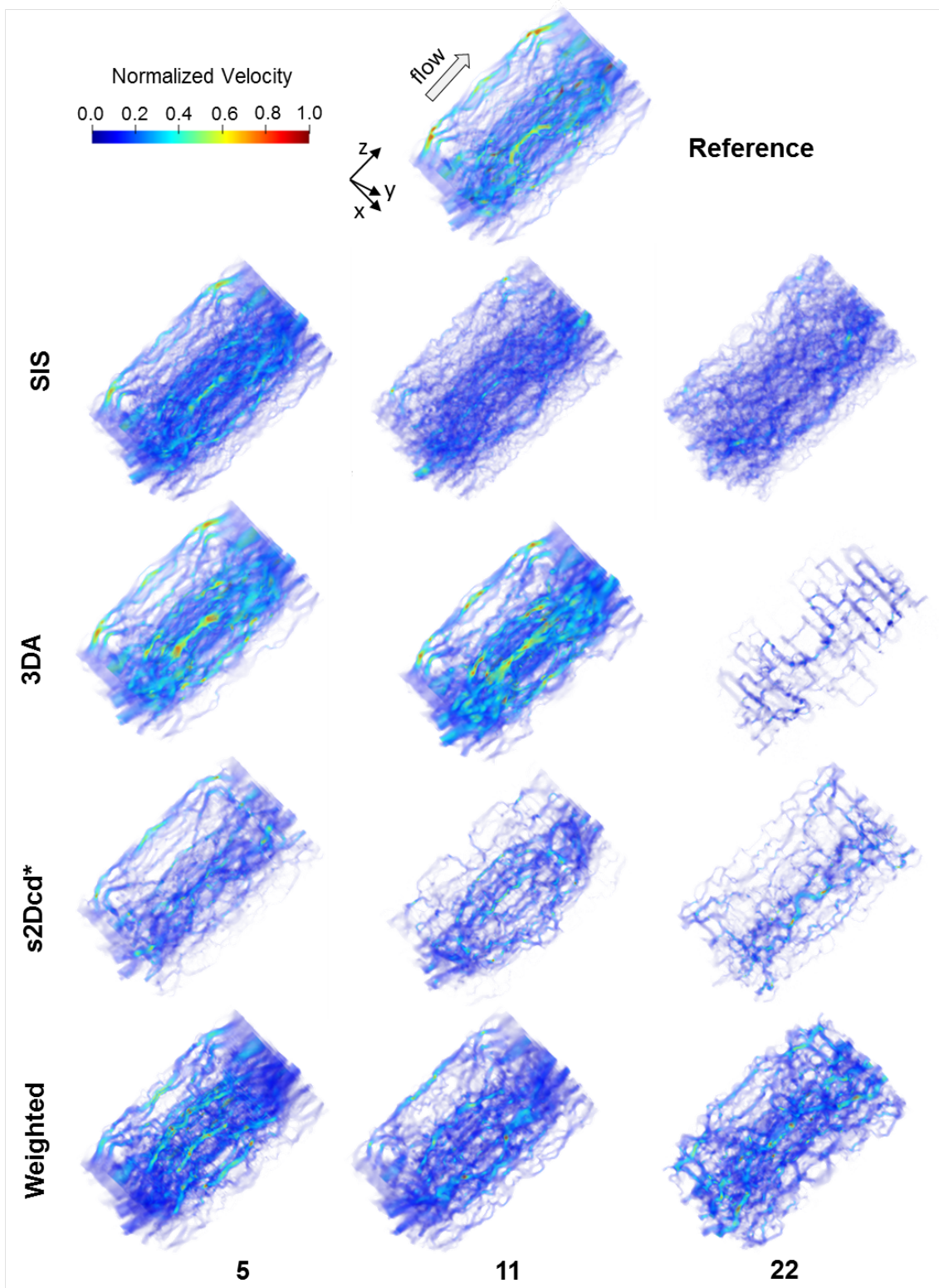


Figure 10 Velocity normalized against maximum velocity for reference and reconstructed samples.

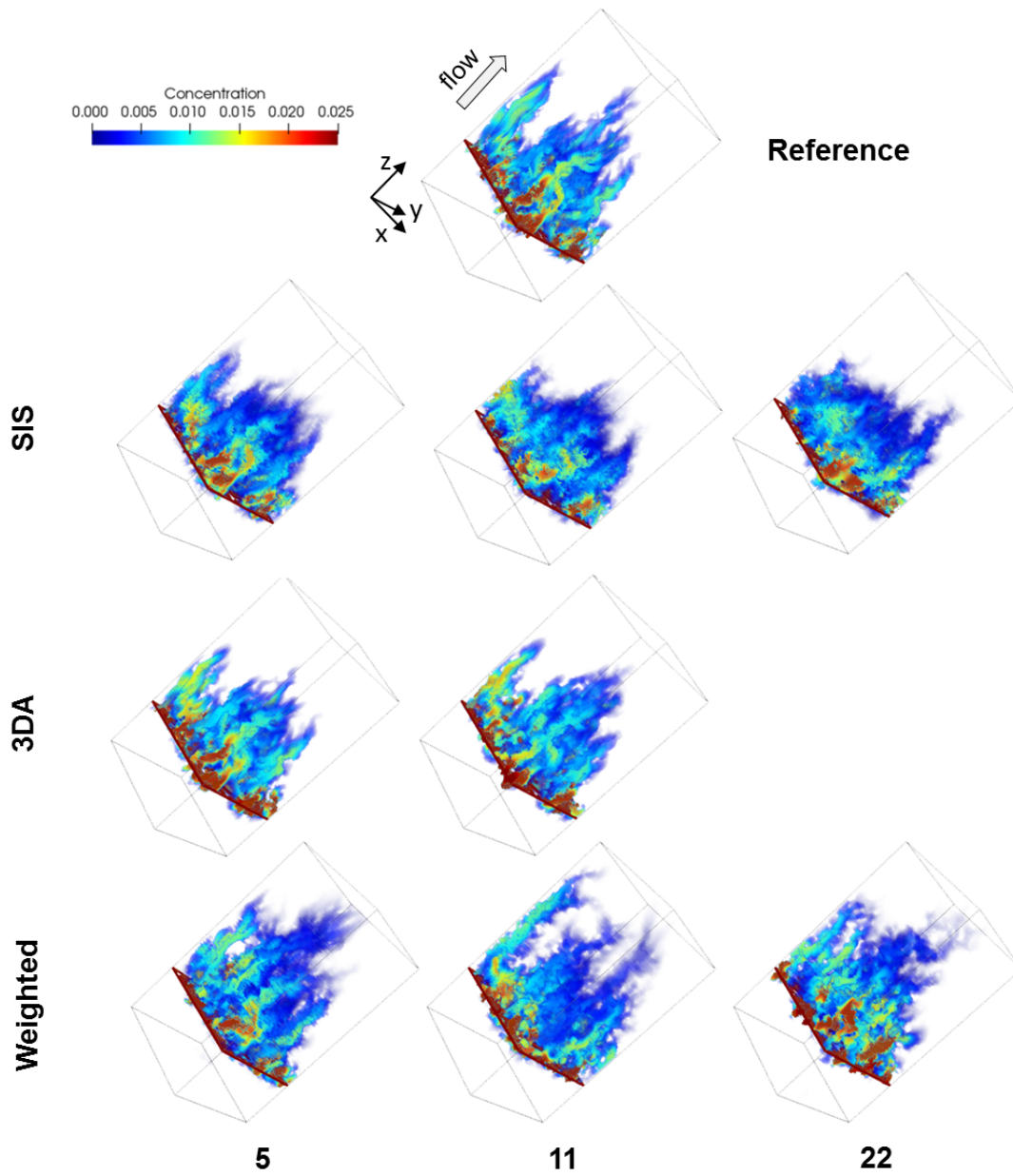


Figure 11 Normalized concentration field at the same given time (10 000 time steps) for reference and reconstructed samples.

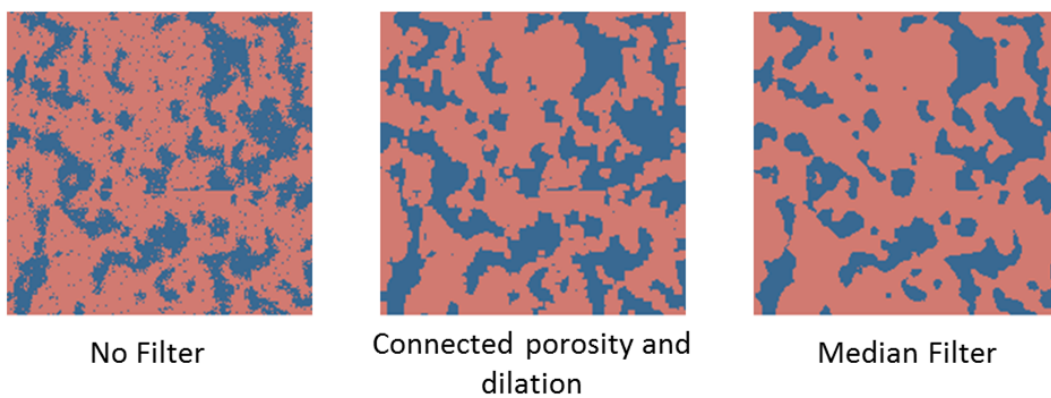


Figure 12 Central xz -slice for a realization considering the weighted-3DA-MPS approach with 11 voxels distance between conditioning slices using different post-processing (no post-processing - left; initially used post-processing - middle; median filter - right)

ACKNOWLEDGEMENTS

The financial support from NEEDS MIPOR is gratefully acknowledged. This work was also partially funded by the ICEEL Carnot Institute (grant MultiEC-HYDRO). We are thankful to Stephane Gaboreau who provided the digital images of the compacted illite used in this article. We also thank Emerson-Paradigm for providing the SKUA-GOCAD software and API.

REFERENCES

- Andrä, H., Combaret, N., Dvorkin, J., Glatt, E., Han, J., Kabel, M., Keehm, Y., Krzikalla, F., Lee, M., Madonna, C., Marsh, M., Mukerji, T., Saenger, E. H., Sain, R., Saxena, N., Ricker, S., Wiegmann, A., Zhan, X., jan 2013a. Digital rock physics benchmarks—Part I: Imaging and segmentation. *Computers & Geosciences* 50, 25–32. (Cited page 1)
- Andrä, H., Combaret, N., Dvorkin, J., Glatt, E., Han, J., Kabel, M., Keehm, Y., Krzikalla, F., Lee, M., Madonna, C., Marsh, M., Mukerji, T., Saenger, E. H., Sain, R., Saxena, N., Ricker, S., Wiegmann, A., Zhan, X., jan 2013b. Digital rock physics benchmarks—part II: Computing effective properties. *Computers & Geosciences* 50, 33–43. (Cited page 1)
- Armstrong, R. T., McClure, J. E., Robins, V., Liu, Z., Arns, C. H., Schlüter, S., Berg, S., oct 2019. Porous Media Characterization Using Minkowski Functionals: Theories, Applications and Future Directions. *Transport in Porous Media* 130 (1), 305–335. (Cited page 6)
- Arpat, G. B., Caers, J., ??? A Multiple-scale, Pattern-based Approach to Sequential Simulation, year = 2004. In: Leuangthong, O., Deutsch, C. V. (Eds.), *Geostatistics Banff 2004*. No. 14 in *Quantitative Geology and Geostatistics*. Springer Netherlands, pp. 255–264. (Cited page 4)
- Bakke, S., Øren, P.-E., jun 1997. 3-D Pore-Scale Modelling of Sandstones and Flow Simulations in the Pore Networks. *SPE Journal* 2 (02), 136–149. (Cited page 2)
- Blunt, M. J., Bijeljic, B., Dong, H., Gharbi, O., Iglauer, S., Mostaghimi, P., Paluszny, A., Pentland, C., jan 2013. Pore-scale imaging and modelling. *Advances in Water Resources* 51, 197–216. (Cited page 1)
- Chen, L., Zhang, L., Kang, Q., Viswanathan, H. S., Yao, J., Tao, W., jul 2015. Nanoscale simulation of shale transport properties using the lattice Boltzmann method: permeability and diffusivity. *Scientific Reports* 5 (1), 8089. (Cited page 2)
- Chen, Q., Mariethoz, G., Liu, G., Comunian, A., Ma, X., 2018. Locality-based 3-D multiple-point statistics reconstruction using 2-D geological cross-sections. *Hydrology and Earth System Sciences Discussions* (June), 1–31. (Cited page 3)
- Comunian, a., Renard, P., Straubhaar, J., mar 2012a. 3D multiple-point statistics simulation using 2D training images. *Computers & Geosciences* 40, 49–65. (Cited pages 2, 3, 4, 5, 7, and 15)
- Comunian, A., Renard, P., Straubhaar, J., mar 2012b. 3D multiple-point statistics simulation using 2D training images. *Computers & Geosciences* 40, 49–65. (Cited page 5)
- Davy, C. A., Adler, P M., dec 2017. Three-scale analysis of the permeability of a natural shale. *Physical Review E* 96 (6), 063116. (Cited page 2)
- Desbois, G., Urai, J. L., Hemes, S., Brassinnes, S., De Craen, M., Sillen, X., sep 2014. Nanometer-scale pore fluid distribution and drying damage in preserved clay cores from Belgian clay formations inferred by BIB-cryo-SEM. *Engineering Geology* 179, 117–131. (Cited page 1)
- Deutsch, C. V., Journel, A. G., 1997. *GSLIB: Geostatistical Software Library and User's Guide* (Applied Geostatistics). Oxford University Press, USA. (Cited page 3)
- Ding, K., Teng, Q., Wang, Z., He, X., Feng, J., Jun 2018. Improved multipoint statistics method for reconstructing three-dimensional porous media from a two-dimensional image via porosity matching. *Phys. Rev. E* 97, 063304. (Cited page 4)
- Dymitrowska, M., Pazdniakou, A., Adler, P M., 2014. Two-phase-flow pore-size simulations in Opalinus clay by the Lattice Boltzmann Method. *Geological Society, London, Special Publications* 400 (1), 195–206. (Cited page 2)
- Gaboreau, S., Robinet, J.-C., Prêt, D., apr 2016. Optimization of pore-network characterization of a compacted clay material by TEM and FIB/SEM imaging. *Microporous and Mesoporous Materials* 224, 116–128. (Cited page 2)
- Garabedian, S. P., LeBlanc, D. R., Gelhar, L. W., Celia, M. A., may 1991. Large-scale natural gradient tracer test in sand and gravel, Cape Cod, Massachusetts: 2. Analysis of spatial moments for a nonreactive tracer. *Water Resources Research* 27 (5), 911–924. (Cited page 8)
- Ginzburg, I., Verhaeghe, F., d'Humieres, D., 2008. Two-relaxation-time lattice boltzmann scheme: About parametrization, velocity, pressure and mixed

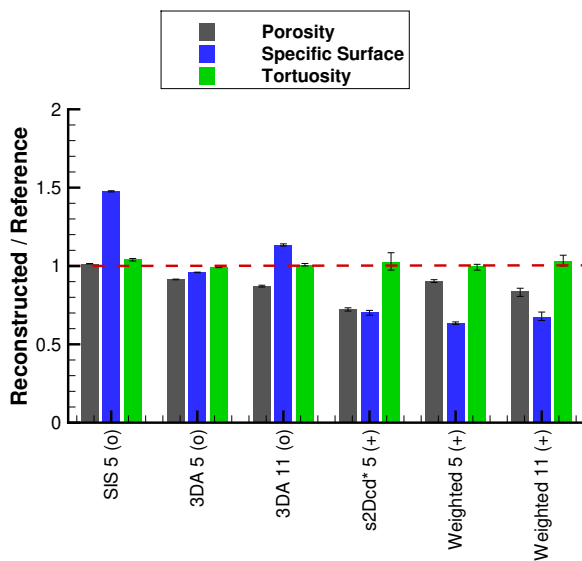


Figure 13 Ratio of a morphological characteristic averaged on all realisations for the reconstructed images to the reference. Error bars indicate variation in between realizations. (o) realizations without post-processing. (+) realizations with median filter.

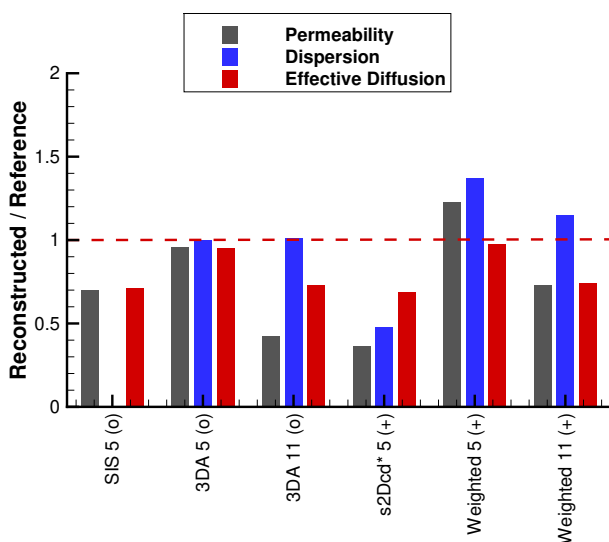


Figure 14 Ratio of effective properties for one realization of the reconstructed images to the reference. (o) realizations without post-processing. (+) realizations with median filter.

- boundary conditions. *Communications in computational physics* 3 (2), 427 – 478. (Cited page 7)
- Gommes, C. J., Bons, A.-J., Blacher, S., Dunsmuir, J. H., Tsou, A. H., aug 2009. Practical methods for measuring the tortuosity of porous materials from binary or gray-tone tomographic reconstructions. *AIChE Journal* 55 (8), 2000–2012. (Cited page 7)
- Guardiano, F. B., Srivastava, R. M., 1993. Multivariate Geostatistics: Beyond Bivariate Moments. In: Soares, A. (Ed.), *Geostatistics* {{Tr{6}ia}} 92. No. 5 in *Quantitative Geology and Geostatistics*. Springer Netherlands, pp. 133–144. (Cited page 4)
- Guibert, R., Nazarova, M., Horgue, P., Hamon, G., Creux, P., Debenest, G., apr 2015. Computational Permeability Determination from Pore-Scale Imaging: Sample Size, Mesh and Method Sensitivities. *Transport in Porous Media* 107 (3), 641–656. (Cited page 1)
- Gunda, N. S. K., Choi, H.-W., Berson, A., Kenney, B., Karan, K., Pharoah, J. G., Mitra, S. K., 2011. Focused ion beam-scanning electron microscopy on solid-oxide fuel-cell electrode: Image analysis and computing effective transport properties. *Journal of Power Sources* 196 (7), 3592 – 3603. (Cited page 5)
- Hajizadeh, A., Safekordi, A., Farhadpour, F. A., 2011. A multiple-point statistics algorithm for 3D pore space reconstruction from 2D images. *Advances in Water Resources* 34 (10), 1256–1267. (Cited pages 2 and 4)
- Hemes, S., Desbois, G., Urai, J. L., Schröppel, B., Schwarz, J.-O., may 2015. Multi-scale characterization of porosity in Boom Clay (HADES-level, Mol, Belgium) using a combination of X-ray μ -CT, 2D BIB-SEM and FIB-SEM tomography. *Microporous and Mesoporous Materials* 208, 1–20. (Cited page 1)
- Holzer, L., Münch, B., Rizzi, M., Wepf, R., Marschall, P., Graule, T., feb 2010. 3D-microstructure analysis of hydrated bentonite with cryo-stabilized pore water. *Applied Clay Science* 47 (3-4), 330–342. (Cited page 1)
- Hu, Q., Ewing, R. P., Dultz, S., may 2012. Low pore connectivity in natural rock. *Journal of Contaminant Hydrology* 133, 76–83. (Cited page 1)
- Journel, A. G., Isaaks, E. H., 1984. Conditional indicator simulation: {{Application}} to a {{Saskatchewan}} uranium deposit. *Journal of the International Association for Mathematical Geology* 16 (7), 685–718. (Cited page 3)
- Ju, Y., Huang, Y., Zheng, J., Qian, X., Xie, H., Zhao, X., 2017. Multi-thread parallel algorithm for reconstructing 3D large-scale porous structures. *Computers and Geosciences* 101 (January), 10–20. (Cited page 2)
- Ju, Y., Zheng, J., Epstein, M., Sudak, L., Wang, J., Zhao, X., 2014. 3D numerical reconstruction of well-connected porous structure of rock using fractal algorithms. *Computer Methods in Applied Mechanics and Engineering* 279, 212–226. (Cited page 2)
- Kamrava, S., Tahmasebi, P., Sahimi, M., oct 2019. Enhancing images of shale formations by a hybrid stochastic and deep learning algorithm. *Neural Networks* 118, 310–320. (Cited page 16)
- Keehm, Y., 2004. Permeability prediction from thin sections: 3D reconstruction and Lattice-Boltzmann flow simulation. *Geophysical Research Letters* 31 (4), L04606. (Cited page 2)
- Legland, D., Arganda-Carreras, I., Andrey, P., jul 2016. MorphoLibJ: integrated library and plugins for mathematical morphology with ImageJ. *Bioinformatics*, btw413. (Cited page 6)
- Lemmens, H.J. and Butcher, A.R. and Botha, P., 2011. FIB/SEM and SEM/EDX: a new dawn for the SEM in the core lab? *Petrophysics* 52 (6), 452 — 456. (Cited page 2)
- Mariethoz, G., Renard, P., 2010. Reconstruction of Incomplete Data Sets or Images Using Direct Sampling. *Mathematical Geosciences* 42 (3), 245–268. (Cited pages 4 and 5)
- Mariethoz, G., Renard, P., Straubhaar, J., 2010. The Direct Sampling method to perform multiple-point geostatistical simulations. *Water Resources Research* 46 (11), W11536–14. (Cited pages 4 and 6)
- Marschall, P., Horseman, S., Gimmi, T., jan 2005. Characterisation of Gas Transport Properties of the Opalinus Clay, a Potential Host Rock Formation for Radioactive Waste Disposal. *Oil & Gas Science and Technology* 60 (1), 121–139. (Cited page 1)
- Mehmani, A., Prodanović, M., jan 2014. The effect of microporosity on transport properties in porous media. *Advances in Water Resources* 63, 104–119. (Cited page 1)
- Münch, B., Holzer, L., dec 2008. Contradicting Geometrical Concepts in Pore Size Analysis Attained with Electron Microscopy and Mercury Intrusion. *Journal of the American Ceramic Society* 91 (12), 4059–4067. (Cited page 7)
- Okabe, H., Blunt, M. J., dec 2007. Pore space reconstruction of vuggy carbonates using microtomography and multiple-point statistics. *Water Resources Research* 43 (12). (Cited pages 2, 3, 4, 5, and 6)
- Øren, P.-E., Bakke, S., 2002. Process Based Reconstruction of Sandstones and Prediction of Transport Properties. *Transport in Porous Media* 46 (2-3), 311–343. (Cited pages 2 and 3)
- Øren, P.-E., Bakke, S., sep 2003. Reconstruction of Berea sandstone and pore-scale modelling of wettability effects. *Journal of Petroleum Science and Engineering* 39 (3-4), 177–199. (Cited page 2)
- Ortega Ramírez, M. P., Oxarango, L., Gastelum Strozzi, A., 2019. Effect of x-ray ct resolution on the quality of permeability computation for granular soils: definition of a criterion based on morphological properties. *Soil Research* 57 (6), 589–600. (Cited page 5)
- Pan, C., Luo, L.-S., Miller, C. T., sep 2006. An evaluation of lattice Boltzmann schemes for porous medium flow simulation. *Computers & Fluids* 35 (8-9), 898–909. (Cited page 7)
- Pazdaniakou, A., Dymitrowska, M., 2018. Migration of Gas in Water Saturated Clays by Coupled Hydraulic-Mechanical Model. *Geofluids* 2018, 1–25. (Cited pages 2 and 7)
- Pazdaniakou, A., Tinet, A.-J., Golfier, F., Kalo, K., Gaboreau, S., Gaire, P., nov 2018. Numerical efficiency assessment of the lattice Boltzmann model for digital nano-porous rock applications. *Advances in Water Resources* 121, 44–56. (Cited page 2)
- Pot, V., Zhong, X., Baveye, P., 2020. Effect of resolution, reconstruction settings, and segmentation methods on the numerical calculation of saturated soil hydraulic conductivity from 3D computed tomography images. *Geoderma* 362, 114089. (Cited page 5)
- Rozenbaum, O., du Roscoat, S. R., may 2014. Representative elementary volume assessment of three-dimensional x-ray microtomography images of heterogeneous materials: Application to limestones. *Physical Review E* 89 (5), 053304. (Cited page 1)
- Salzer, M., Prill, T., Spetl, A., Schladitz, K., Schmidt, V., Jeulin, D., 2015. Quantitative comparison of segmentation algorithms for fib-SEM images of porous media. *Journal of Microscopy* 257 (1), 23 – 30. (Cited page 5)
- Scholz, C., Wirner, F., Götz, J., Rüde, U., Schröder-Turk, G. E., Mecke, K., Bechinger, C., dec 2012. Permeability of Porous Materials Determined from the Euler Characteristic. *Physical Review Letters* 109 (26), 264504. (Cited page 6)
- Shiota, E., Mukunoki, T., Oxarango, L., Tinet, A.-J., Golfier, F., 2019. Micro- and macro-scale water retention properties of granular soils: contribution of the X-Ray CT-based voxel percolation method. *Soil Research*. (Cited page 1)
- Song, W., Yao, J., Ma, J., Couples, G., Li, Y., oct 2017. Assessing relative contributions of transport mechanisms and real gas properties to gas flow in nanoscale organic pores in shales by pore network modelling. *International Journal of Heat and Mass Transfer* 113, 524–537. (Cited page 2)
- Song, Y., Davy, C., Troadec, D., Blanchenet, A.-M., Skoczylas, F., Talandier, J., Robinet, J., aug 2015. Multi-scale pore structure of CO_x clastone: Towards the prediction of fluid transport. *Marine and Petroleum Geology* 65, 63–82. (Cited page 1)
- Straubhaar, J., Renard, P., Mariethoz, G., Froidevaux, R., Besson, O., apr 2011. An Improved Parallel Multiple-point Algorithm Using a List Approach. *Mathematical Geosciences* 43 (3), 305–328. (Cited pages 4 and 6)
- Strebelle, S., 2002. Conditional Simulation of Complex Geological Structures Using Multiple-Point Statistics. *Mathematical Geology* 34 (1), 1–21. (Cited page 4)
- Strebelle, S., Payrazyan, K., Caers, J., sep 2002. Modeling of a Deepwater Turbidite Reservoir Conditional to Seismic Data Using Multiple-Point Geostatistics. In: *SPE Annual Technical Conference and Exhibition*. No. SPE 77425. Society of Petroleum Engineers, New Orleans, p. 10. (Cited page 4)
- Tahmasebi, P., 2017. Structural adjustment for accurate conditioning in large-scale subsurface systems. *Advances in Water Resources* 101, 60 – 74. (Cited page 16)
- Tahmasebi, P., 2018. *Multiple Point Statistics: A Review*. Springer International Publishing, Cham, pp. 613–643. (Cited pages 2, 4, and 16)
- Tahmasebi, P., Sahimi, M., feb 2013. Cross-Correlation Function for Accurate Reconstruction of Heterogeneous Media. *Physical Review Letters* 110 (7), 078002. (Cited pages 2 and 4)
- Tahmasebi, P., Sahimi, M., Andrade, J., 2017a. Image-based modeling of granular porous media. *Geophysical Research Letters* 44, 4738 – 4746. (Cited pages 2 and 3)
- Tahmasebi, P., Sahimi, M., Andrade, J. E., may 2017b. Image-based modeling of granular porous media. *Geophysical Research Letters* 44 (10), 4738–4746. (Cited page 4)
- Tahmasebi, P., Sahimi, M., Kohanpur, A. H., Valocchi, A., 2017c. Pore-scale simulation of flow of CO₂ and brine in reconstructed and actual 3D rock cores. *Journal of Petroleum Science and Engineering* 155, 21 – 33, energy Frontier Research Centers for Investigating Carbon Sequestration. (Cited page 1)
- Wei, M., Liu, Y., Liu, J., Elsworth, D., Zhou, F., apr 2019. Micro-scale investiga-

- tion on coupling of gas diffusion and mechanical deformation of shale. *Journal of Petroleum Science and Engineering* 175, 961–970. (Cited page 2)
- Wildenschild, D., Sheppard, A. P., jan 2013. X-ray imaging and analysis techniques for quantifying pore-scale structure and processes in subsurface porous medium systems. *Advances in Water Resources* 51, 217–246. (Cited page 1)
- Wu, K., Dijke, M. I. J. V., Couples, G. D., Jiang, Z., Ma, J., Sorbie, K. S., Crawford, J., Young, I., Zhang, X., 2006. 3D Stochastic Modelling of Heterogeneous Porous Media – Applications to Reservoir Rocks. *Transport in Porous Media* 65, 443–467. (Cited pages 2 and 3)
- Wu, Y., Lin, C., Ren, L., Yan, W., An, S., Chen, B., Wang, Y., Zhang, X., You, C., Zhang, Y., mar 2018. Reconstruction of 3D porous media using multiple-point statistics based on a 3D training image. *Journal of Natural Gas Science and Engineering* 51, 129–140. (Cited page 2)
- Xu, L., Liu, X., Liang, L., nov 2014. A pore network model reconstruction method via genetic algorithm. *Journal of Natural Gas Science and Engineering* 21, 907–914. (Cited page 3)
- Yang, J., Chu, X., 2013. Quantification of the spatio-temporal variations in hydrologic connectivity of small-scale topographic surfaces under various rainfall conditions. *Journal of Hydrology* 505, 65–77. (Cited pages 8 and 11)
- Yang, Y., Yao, J., Wang, C., Gao, Y., Zhang, Q., An, S., Song, W., nov 2015. New pore space characterization method of shale matrix formation by considering organic and inorganic pores. *Journal of Natural Gas Science and Engineering* 27, 496–503. (Cited page 2)
- Zhang, T., Switzer, T., Journel, A. G., 2005. Sequential Conditional Simulation Using Classification of Local Training Patterns. In: Leuangthong, O., Deutsch, C. V. (Eds.), *Quantitative Geology and Geostatistics*, vol 14. Springer, Dordrecht, pp. 265–273. (Cited page 4)
- Zhu, L., Zhang, C., Zhang, C., Zhou, X., Zhang, Z., Nie, X., Liu, W., Zhu, B., 2019. Challenges and prospects of digital core-reconstruction research. *Geofluids* 219, ID 7814180. (Cited pages 2 and 5)